# Global View of Ionospheric Disturbance Impacts on Kinematic GPS Positioning Solutions during the 2015 St Patrick's Day Storm

Zhe Yang[1], Y. Jade Morton[1], Irina Zakharenkova[2,3], Iurii Cherniak[2], Shuli Song[4], Wei Li[4]

1. Smead Aerospace Engineering Sciences Department, University of Colorado, Boulder, CO, USA
2. COSMIC Program Office, University Corporation for Atmospheric Research, Boulder, CO, USA
3. IZMIRAN, Kaliningrad, Russia
4. Shanghai Astronomical Observatory, Chinese Academy of Sciences, Shanghai, China

**Key Points:**

- Ionospheric disturbances caused high-precision GPS positioning degradation on a global scale during the 2015 St Patrick's Day storm;
- At high latitudes, severe position degradation was observed around magnetic noon and midnight coinciding with plasma irregularities zone;
- At low latitudes, position errors were due to storm-induced plasma bubbles, EIA enhancement, and travelling ionospheric disturbances;

# Abstract

The 2015 St. Patrick's Day geomagnetic storm caused numerous disturbances of the ionosphere, particularly, plasma irregularities, large-scale travelling ionospheric disturbances (LSTIDs), and equatorial ionization anomaly (EIA) enhancement. This study for the first time quantifies the global-scale impacts of the ionospheric disturbances on Global Positioning System (GPS) precise point positioning (PPP) solutions during this extreme space weather event by taking advantage of 5500+ GNSS stations installed worldwide. The overall impact was more severe at high latitudes, while PPP degradation at low latitudes was associated with different types of ionospheric disturbances. Specifically, our results show that kinematic PPP solutions degraded following an intensified auroral particle precipitation during the storm's main phase (06-23 UT) when up to ~70% of the high-latitude stations experienced degraded position solutions in the multi-meter range at 16-18 UT. Around magnetic noon and midnight, the storm-induced plasma irregularities caused notable PPP errors (>10 m) at high latitudes. Interhemispheric differences were observed with a more severe impact seen in the Southern Hemisphere, where PPP outage lasted for ~12 hours during the second main phase (12-23 UT). At low latitudes, post-sunset equatorial plasma irregularities were supressed across most longitudes, but large PPP errors (>2 m) associated with storm-induced plasma bubbles were registered at the Indian sector at 14-18 UT. The storm-induced EIA enhancement and LSTIDs were responsible for the low-latitude PPP degradation at dayside sectors. This study fills the research gap between physical and practical aspects of severe ionospheric storm effects.

# 1. Introduction

Geomagnetic storms are major disturbances in the Earth's magnetic field that occur when solar winds compress the magnetosphere (Gonzalez et al., 1994). They can last from hours to days and affect global dynamics and structures of the Earth's ionosphere/thermosphere. During geomagnetic storms, there are dramatic increases of solar and magnetospheric energy inputs to the upper atmosphere. The energy input taking the form of enhanced electric fields, currents, and energetic particle precipitation perturbs the ionosphere through high-latitude ionization, Joule and particle heating, ion-drag forcing, and disturbed electric field penetration, producing ionospheric storms (Buonsanto, 1999). Investigations of ionospheric storm effects are of fundamental importance in space weather research (e.g., Richmond and Lu, 2000; Kelley et al., 2011; Liu and Wan, 2018 and references therein) for a better understanding of the storm time geospace system. They also have practical significance in quantifying their impacts on ground- and space-based technological systems (e.g., Basu et al., 2008; Astafyeva et al., 2014; Morton, 2014).

Numerous disturbances in the polar, middle, and low latitude ionosphere have been reported in association with ionospheric storms. Ionospheric plasma irregularities, typically characterized as enhancements or depletions of the ionospheric electron density, have attracted much interest in the study of ionospheric storm effects. Their occurrences in the ionospheric F region are generally dominant at high and low latitudes, but behave distinctively during geomagnetic storms. At high latitudes, intense plasma irregularities associated with polar cap patches and polar tongues of ionization are consequences of enhanced particle precipitation, electrostatic turbulence, and plasma instabilities under disturbed geomagnetic conditions (e.g., Tsunoda, 1988; De Franceschi et al., 2008; Moen et al., 2013; Cherniak et al., 2015). At low latitudes, equatorial plasma irregularities/bubbles (EPI/EPB) are triggered or suppressed during geomagnetically disturbed times, which are due mostly to the combined effects of relatively short-lived prompt penetration and longer lasting disturbance dynamo electric fields on equatorial plasma drifts (e.g., Martinis et al., 2005; Fejer et al., 2007; Abdu et al., 2009; Huang, 2018 and references therein). By contrast, mid-latitude irregularities are less severe, and they are usually attributed to expansion of auroral and/or equatorial irregularities under disturbed conditions. It has been suggested that the storm influence on the development of plasma irregularities depends on the phase of the storm (e.g., Abdu, 1997), longitudes (e.g., Li et al., 2010b), and varies from storm to storm (e.g., Basu et al., 2001).

Large-scale travelling ionospheric disturbances (LSTIDs) are another storm-related disturbance that has been investigated extensively. They are generally recognized as ionospheric manifestations of acoustic gravity waves generated at the onset of geomagnetic storms by high-latitude sources, such as Joule heating, Lorentz forces, or intense particle precipitations (Hocke and Schlegel, 1996). Originating from auroral regions, the LSTIDs propagate from high to low latitudes in a global scale, and typically have a period of 30-120 minutes and wavelength longer than 1000 km. The signature of LSTIDs at low latitudes may create conditions for seeding of equatorial plasma irregularities (e.g., Nicolls and Kelley, 2005). Statistical analysis has shown that their occurrences and propagation characteristics (e.g., wavelength, phase velocity, period and direction) are closely related to the magnitude of geomagnetic disturbances (e.g., Afraimovich et al., 2001; Tsugawa et al., 2004; Ding et al., 2008), and show differences between the Northern Hemisphere (NH) and Southern Hemisphere (SH). In addition, other disturbances associated with geomagnetic storms have also been studied, such as enhancement/suppression of the equatorial ionization anomaly (EIA) process (e.g., Mannucci et al., 2005; Zhao et al., 2008; Kuai et al., 2016 and references therein). The completely different disturbance behavior indicates that the ionospheric storm effects are complex. The increase and decrease in electron density during the storms typically represent the simplest classification of ionospheric disturbances, known as positive and negative storm effects, respectively.

Much persistent efforts have been made using observations from radio communication/navigation systems to associate the observations with the sources and drivers, as well as the coupling between regions. On the practical side, however, to our best knowledge, there has not been a comprehensive study of ionospheric disturbance impacts during a geomagnetic storm on applications of space-based radio systems, such as the Global Positioning System/Global Navigation Satellite System (GPS/GNSS). Among ionospheric disturbances, it is generally believed that the ionospheric plasma irregularities can adversely impact GNSS applications through two mechanisms: scintillation and ranging error. Ionospheric scintillation is due to scattering or diffraction of the signal by the plasma structure. Its symptoms are rapid fluctuations in signal amplitude and/or phase (Kintner et al., 2007). Ionospheric scintillation can lead to a GPS receiver being unable to track one or more visible satellite signals for a considerable length of time (Jiao and Morton, 2015). The ranging error is due to the steep gradient of refractive effects of the ionospheric total electron content (TEC) (Basu et al., 2001).

The gap between the physical and practical aspects regarding ionospheric storm research still remains. The aim of this paper is to address this gap by focusing on a simultaneous global overview of several types of ionospheric disturbances occurring during a severe geomagnetic storm and their impact on GPS positioning solutions for high-precision applications. We focus on the March 17, 2015 storm by analyzing 5500+ globally distributed GNSS stations measurements. As the strongest geomagnetic storm of the 24th solar cycle so far, a considerable number of researchers have investigated the ionospheric disturbances associated with this storm, such as high-/middle-latitude plasma irregularities (e.g., Cherniak et al., 2015; Prikryl et al., 2016; Heine et al., 2017), EPBs (e.g., Carter et al., 2016; Zhou et al., 2016), LSTIDs (e.g., Yao et al., 2016; Zakharenkova et al., 2016), and other positive/negative storm effects (e.g., Astafyeva et al., 2015; Kuai et al., 2016). These studies have been carried out at both regional and global scales. A collection of studies about the geospace response to this super storm are summarized in Zhang et al., (2017).

The key objective of this study is to ascertain the impacts of the storm-induced ionospheric disturbances on kinematic GPS precise point positioning (PPP) from an unprecedented number of globally distributed GPS/GNSS stations. These new results are highly valuable for estimation of scintillation threat and prediction impacts of severe geomagnetic storms on GNSS-based kinematic applications at different latitudinal zones. Further, it fills the research gap from the point of view of global ionospheric storm effects on GNSS applications.

# 2. Data and Methodology

## 2.1 GPS data

GPS data at a sampling rate of 30 sec from 5500+ GNSS stations are processed for characterizing ionospheric disturbances and solving kinematic PPP solutions for 17-18 March 2015. These GNSS stations are provided by a number of regional and global networks. Figure 1 presents the geographic location of the globally distributed GNSS stations used in this study. It is clear that the coverage of GNSS stations in North and South America, Europe, eastern Asia, and Australia is better than that in other regions. Among the 5500+ stations, 4791 and 657 stations are in the Northern Hemisphere (NH) and Southern Hemisphere (SH), respectively.

## 2.2 Ionospheric disturbance index

The GPS data from globally distributed stations provide the measurements of TEC to characterize ionospheric density. In the studies of global-scale ionospheric disturbances related to the March 2015 storm, Astafyeva et al. (2015) used the vertical TEC for studying signatures of positive and negative storms around the globe; Zakharenkova et al. (2016) adopted the detrended TEC to derive the LSTID-related perturbations, while Yao et al. (2016) exploited the rate of change of TEC index (ROTI) and the second-order TEC difference operator to investigate the characteristics of TIDs. The number of the GPS stations used for this study is greater than that used in these previous studies.

In the present study, we use the ROTI metric derived from GPS dual-frequency carrier phase measurements to characterize ionospheric irregularity occurrences. Defined as the standard deviation of the rate of TEC, the ROTI is an indicator generally used for quantifying small-scale ionospheric plasma irregularities (e.g.,Pi et al., 1997; Cherniak et al., 2014, 2018; Yang and Liu, 2018). Because small-scale plasma irregularities are expected to generate significant scintillation effects on GPS signals, we use the ROTI to characterize severe ionospheric plasma density irregularities and their impacts on kinematic PPP solutions throughout our analysis. In this study, ROTI is calculated at a 30 sec rate over 5 min. It is mapped onto ionospheric piercing points (IPPs) at an altitude of 350 km.

## 2.3 Kinematic PPP processing

The GPS carrier phase and pseudorange measurements are processed for kinematic PPP solutions by utilizing routines in the Real-Time Kinematic Library (RTKLIB). RTKLIB is an open source program package for GNSS positioning and has been applied for deformation detections caused by earthquakes (e.g., Ohta et al., 2012 and references therein). To obtain high-precision kinematic PPP solutions, error corrections were made in GPS observations, including those related to atmosphere (ionosphere and troposphere), satellite (e.g., clock, orbit and antenna phase offset), receiver (e.g., phase wind-up error and antenna phase offset), and geophysical factors (e.g., pole tides, solid earth tides). The ionospheric refraction effect is corrected by forming an ionosphere-free linear combination. Under normal conditions, a centimeter- to decimeter-level accuracy for the receiver position can be achieved with those-above mentioned error corrections. In our study, the kinematic positions of the globally distributed GNSS receivers are obtained every 30 sec. An elevation cut-off angle of 20° is used to optimize the satellite geometry for the position calculation and to minimize multipath effects on the ROTI estimation. The position solutions are evaluated by a comparison with their daily solutions in static PPP mode on 16 March 2015. Their position errors are further examined in association with the storm-induced ionospheric disturbances.

# 3. Results and Discussion

## 3.1 Overview of ionospheric disturbances and kinematic PPP error

The March 2015 storm occurred on the St. Patrick's Day, 17 March, following a coronal mass ejection impact. It has so far been the strongest storm in the 24th solar cycle. Figure 2 depicts the temporal variations of selected interplanetary parameters (interplanetary magnetic field (IMF) By, Bz components) and geomagnetic indices (Kp, SYM-H, and auroral electrojet (AE) index). Bottom panels show the horizontal and vertical components of kinematic PPP errors combined for all considered GNSS stations during 17-18 March 2015. The storm sudden commencement (SSC) occurred at ~04:45 universal time (UT) on 17 March 2015. After 05-06 UT, the SYM-H index started to gradually decrease with several minima of -93 and -150 nT at ~09:40 and ~16:30 UT, respectively. At about 23:00 UT, the SYM-H index reached its minimum value of -233 nT, meaning that the main phase lasted for ~17h. After that, the storm went into the recovery phase, which lasted for few more days.

During the main phase of the storm (i.e., 05:00-23:00 UT), the IMF Bz switched between north and south before settling for southward between 12:20 UT and 22:30 UT during which the planetary Kp index reached a maximum value of 8-. The AE index had several intensification peaks at ~09:00, ~14:00, and during 17-24:00 UT. The kinematic PPP errors, as shown in Figure 2b-2c, showed a significant increase in both horizontal and vertical components during the main phase. The statistical standard deviation of the PPP errors generally varied within ±0.1 m before SSC and during the recovery phase. During the geomagnetically disturbed period, however, it went up to 1 m, and greater values were seen in the vertical component, especially during 16:00-18:00 UT. Our following analysis reveals that the degradation in the PPP accuracy are associated with the storm-induced ionospheric disturbances.

Figure 3 illustrates global maps of ROTI and kinematic three-dimensional (3-D) PPP errors as a function of geographic longitude and latitude, obtained using 5500+ GNSS stations. The maps with a 3h time resolution present their temporal variations during 17-18 March, and the grey shades on each map represent the nightside. Movies S1-S2 and S3-S4 (5 min resolution) in supporting information show a more detailed temporal-spatial evolution of the ionospheric plasma irregularities and 3-D PPP errors on 17-18 March 2015, respectively. We note that occurrence of strong plasma irregularities during the storm coincided with significant degradation of the performance of kinematic PPP, and such impacts vary at different time periods of the storm. During the pre-storm period (00:00-04:00 UT), ionospheric plasma irregularities indicated by the ROTI were mainly observed at high latitudes of North America and Antarctic, as well as at low latitudes of South America (a typical occurrence of intense post-sunset EPIs during March season). After ~04:45 UT, the increased geomagnetic activity led to ionospheric disturbances of various types, scales, and geographical location, which can potentially contribute to degradations in the PPP solutions.

Some notable features observed during the main phase of the storm are described below, according to Figure 3 and Movies S1 and S3. During the three time periods, i.e., 06:00-10:00, 12:30-19:00, and 20:00-24:00 UT, the high-latitude plasma irregularities expanded equatorward beyond 50°N magnetic latitude in both hemispheres. As a consequence, a prominent increase in the 3-D position error extends from high down to middle latitudes. The most notable degradations (>1 meter) are found after 13:00 UT, particularly during 16:00-18:00UT when intensified plasma irregularities were observed simultaneously at middle and high latitudes of both hemispheres. The ionospheric response during those periods corresponds well with the variations of the AE index, which represents the magnetospheric energy input (e.g., Joule heating and Lorentz force) to the polar region. At low latitudes, with the exception of localized post-sunset EPIs at Australian and Indian region during 09:00-18:00 UT, we observe mainly suppression of post-sunset EPIs. However, the position errors at equatorial/low latitudes show relatively high values even at local daytime. A large PPP degradation is observed during 06:00-11:00 UT and 14:00-20:00 UT at low latitudes of the Asian-Australian and America sectors, respectively.

Figure 4 depicts the temporal variations of ROTI and the position errors in corrected geomagnetic (CGM) latitude. The CGM coordinates of a given geographic location are determined by tracing the magnetic field line from the location to the Earth-centered dipole equator defined by the International Geomagnetic Reference Field (IGRF) (Heres and Bonito, 2007). They were defined for the purpose of understanding geophysical phenomena within the context of a geomagnetic framework. In this study, we use altitude adjusted CGM coordinates to describe the ionospheric disturbances and their impacts. The ROTI is mapped at IPP points while the position errors are represented at the stations' locations.

Clearly, after the storm onset the intense ionospheric plasma irregularities occurred at the auroral regions of both hemispheres (Figure 4a). During the main phase, they expanded to lower magnetic latitudes. The PPP degradations (Figure 4b) correlate well with the development of auroral plasma irregularities during the storm, while at the equatorial region (within ±20° magnetic latitude) large PPP errors occurred even during suppression of post-sunset EPIs (Figure 4a). Figure 4c shows the percentage of GNSS stations with position errors exceeding 1 meter which strongly correlated with the AE index, with a maximum of ~70% being observed at high latitudes during 16:00-18:00 UT. This effect mainly related with gradual extension of auroral oval after particles precipitation intensification when area of strong ionospheric irregularities cover more stations and affect their position accuracy.

Below, we present the observations at different latitude and longitude sectors for both polar and low-latitude regions, during and after the storm, to investigate the storm-related impacts on the high-precision PPP in a more detailed way.

## 3.2 High-latitude disturbances and kinematic PPP error

At high latitudes, intense ionospheric plasma irregularities since SSC led to a dramatic increase in the kinematic PPP errors, as observed from Figure 3 and Figure 4. We investigated in detail the temporal-spatial evolutions of high-latitude plasma irregularities at both hemispheres and their impacts on the PPP errors with the storm progression by taking advantage of the GPS observations within 40°-90° MLAT.

### 3.2.1 Northern Hemisphere Response

In the northern hemisphere (NH), there are ~3250 GNSS stations within 40°-90°N MLAT. Based on their measurements, Figure 5a-5f depicts the polar view maps of ROTI (a and d), 3-D PPP errors (b and e) and occurrence rates of the 3-D error exceeding 1 meter (c and f) as a function of the CGM latitude and magnetic local time (MLT) in the NH during and after the geomagnetic storm, respectively. Figure 5g-5h presents the PPP error distributions over UT and MLT during and after the storm. Note that in each polar map the ROTI is projected onto the IPPs (CGM latitude) at ~350 km altitude, whereas the position errors are based on the geomagnetic locations of GNSS stations. Their values are averaged in a bin of 5 min MLT x 2° CGM latitude, and the occurrence rate of the large position error (>1m) is defined as the number of cases relative to the total number of data points in each bin.

The daily ROTI maps for the NH polar region reveal the evolution of plasma irregularities near and within the auroral zone. During the storm (Figure 5a), the irregularity oval expanded equatorward and poleward in response to disturbed geomagnetic activity. The farthest equatorward edge was detected at around 50°N between 15-17 MLT, while the enhanced irregularity intensity primarily registered within 60°N, 21- 06 MLT and 11-13 MLT. The enhancement had poleward structure from local noon to midnight.

The storm-induced strong plasma irregularities resulted in large errors in the high-precision PPP solutions for the ground-based stations (Figure 5b). The PPP degradation occurs in a broader range of the CGM latitude (down to 40°N) compared to the ROTI disturbances. This is because the GPS receiver positioning solution requires measurements from four or more satellites in view distributed within a broader region (~$10^{o}$ latitude and longitude) centered around the receiver.

Position errors >1 m occurred corresponding to the development of ionospheric irregularities within the auroral oval (Figure 5c). Their maximum occurrence was mostly at the equatorward edge of the nightside irregularities oval around 60°N, as well as within 70°-80°N at 12-18 MLT. After the storm (Figures 5d-5f), the plasma irregularities were seen at all MLT sectors, but their regions of impact are confined within 70°-80°N on the dayside, while within 60°-70°N on the nightside.

The error distribution summarized in Figure 5g and 5h suggests the UT and MLT dependence of severe PPP degradation. As illustrated, the position error generally varied below 2 m, but in the UT frame greater errors occur after SSC during the AE intensification periods of 07-12 and 14-24 UT. In the MLT frame, PPP error greater than 5 m mostly happened at around magnetic noon, (12-14 MLT) and midnight periods (20-24 MLT).

### 3.2.2 Southern Hemisphere Response

In the SH, there are ~220 GNSS stations distributed within 40°-90°S CGM latitudes, much less than that in the NH. Figure 6 presents the polar view maps of ROTI and PPP position errors (a-f) and the position error distributions as a function of UT and MLT (g-h) during 17-18 March in the SH. As shown, the occurrence of plasma irregularities in the SH was also detected within and near the auroral oval with considerable equatorward and poleward expansions on the storm day. However, their evolution and the induced PPP degradation are different from those observed in the NH.

During the storm, the increased intensity of the irregularities (Figure 6a) in the SH was mainly observed during the late night 04-06 MLT and in the noon sector of 09-15 MLT, poleward from ~50°S MLAT. The oval exhibited a very distinct poleward expansion in the noon sector. Along the intensified irregularities patterns, PPP solutions degraded at all MLT sectors and extended to 40°-50°S MLAT (Figure 6b). The large position error (>1 m) was observed where the irregularities intensified during 04-06 and 09-15 MLT (Figure 6c). Due to the lack of GPS stations in the SH, the position degradation cannot be observed near the south magnetic pole.

After the storm (Figure 6d), the irregularity oval was weakened and was restricted mainly within 70°-80°N on the dayside period of 06-15 MLT and within 60°-75°N on the nightside (18-00 MLT). Correspondingly, the PPP degradation was confined within 60°S MLAT and the large error (> 1 m) mostly occurred in the afternoon sector (18-00 MLT) (Figures 6e and 6f).

Figures 6g and 6h indicate that the PPP error in the SH is below 5 m during the storm, which is greater than that (<2 m) observed in the NH (Figures 5g and 5h). Similar features can be observed on the UT and MLT dependence of severe PPP degradation (>5 m) on the storm day at both SH and NH. One observation is that severe degradation was prominent during the periods of increased auroral activity, e.g., 07-12 and 14-24 UT. Another common feature is that the most outstanding degradation (> 10m) was seen during the noon period (12-16 MLT) and around midnight (20-24 MLT).

### 3.2.3 Explanations of Observed SH and NH Responses

Cherniak et al. (2015) first reported the dynamics of ionospheric plasma during the St. Patrick storm using observations from ~2700 GPS stations. Some of the patterns of the high-latitude ionospheric irregularities observed in this study can be explained based on their analysis. The intense irregularities shown in the daily ROTI maps (Figure 5a and Figure 6a) were related to the storm-induced gradient of the plasma density caused by auroral particle precipitation and plasma flows. Their poleward structure from noon to midnight was associated with the formation of the storm enhanced density/tongue of ionization (SED/TOI) structures and further evolution to large-scale polar cap patches. The time periods (i.e., 07-12 UT, and 14-24 UT) when notable position degradation (>5 m) was seen corresponded with that of rapid increase of intense irregularities associated with enhanced auroral particle precipitation. At ~12-13 UT, less position degradation was observed due to the decrease of intense irregularities initiated by the northward turn of the IMF Bz.

Severe PPP degradations (>10 m) at high latitudes around magnetic noon and midnight are closely coincident with intense high-latitude phase scintillation occurrence associated with auroral particle precipitations and horizontal transportation of SED/TOI structures as observed at NH (Cherniak et al., 2015) and SH (Cherniak and Zakharenkova, 2016). At high latitudes, scintillations are strongly controlled by magnetic field activity. During geomagnetic storms, scintillations appear at the edges of large-scale irregularities (e.g., SED and polar cap patches) with a steep density gradient (e.g., Mitchell et al., 2005; Prikryl et al., 2010; Wang et al., 2016). They have the greatest occurrence around magnetic noon and magnetic midnight, as pointed out by several statistical analyses (e.g., Li et al., 2010a; Jin et al., 2015). GPS signal scintillation may cause carrier phase measurement cycle slips or receiver loss of signal lock. This results in large errors in the PPP solutions. The PPP errors validate the significant effects of the scintillation occurrence at high latitude.

### 3.2.4 High Latitude Spatial Expansion Analysis

Figures 5 and 6 confirm that the storm-induced plasma irregularities had a significant spatial expansion. The spatial expansion can be more clearly observed by examining measurements at two chains of GPS stations along longitude in both hemispheres, as shown in Figures 7a and 7b. In the NH, two longitude chains are selected at 85°W and 10°E over North America and Europe, respectively. In the SH, the two chains were selected along 65°W and 170°E over South America and New Zealand, respectively. For each chain, 5-7 GPS stations within 30°-90° geographic latitude (GLAT) were selected.

Figures 7c-7f show latitudinally sliced maps of ROTI as a function of time from 00-24 UT on 17-18 March 2015, while Figures 7g-7j depict the corresponding variability of the position errors for the selected stations. The figure shows that the plasma irregularities were intensified with a significant equatorward expansion during the periods of increased auroral activity, i.e., 07-12 and 17-24 UT. Correspondingly, the increased PPP degradation or even outages were found. Compared with the NH, the PPP degradation was more severe in the SH, despite the sparse station coverage.

In the NH, increased position error was frequently seen at high latitudes during the main phase of the storm, but at mid-latitudes it primarily happened after 12 UT. Along the North American chain, the ROTI enhancement (Figures 7c and 7g) started at ~07 UT (local night) and continued until the end of the storm day. Equatorward expansion to 40°-45°N geographic latitude (50°-55°N MLAT) was observed during 07-12 UT and 22-24 UT. This caused the stations above 40°N GLAT to have large position errors after SSC. In comparison, along the European chain (Figures 7d and 7h), the ROTI enhancement began after ~12 UT and lasted till ~24 UT. Their expansion was less far equatorward, only reaching ~50°-60°N GLAT (45°-50°N MLAT) at ~17-24 UT. However, during 17-24 UT, the position degradation was also seen at mid-latitudes below 50°N. After the storm, the PPP solution was less degraded, which corresponds to much weaker plasma irregularities within the auroral zone.

In the SH, the South American chain shows larger position errors. The large ROTI along this chain (Figures 7e and 7i) started at ~07 UT and had a significant equatorward expansion toward ~60°-70°S GLAT over the entire periods of increased auroral activity. This led to an increased position errors during 07-12 UT and PPP outage at high-latitude stations from 12 UT to 24 UT. Severe degradation happened during 13-17 UT for mid-latitude stations (~30-45°S GLAT and 20-30°S MLAT). Likewise, along the New Zealand chain (Figures 7f and 7j), the PPP was degraded during 07-12 UT, and outage occurred after ~12 UT during the irregularity expansion (~55°S GLAT). After the storm, the PPP solutions along both chains became available, indicating that the storm-induced plasma irregularities caused the receiver loss of the GPS signal lock for a long period of time (~12 hours).

Cherniak et al. (2015) emphasized that the observed equatorward expansion at different sectors was due to the development of various irregular plasma structures. In the Western Hemisphere (e.g., North and South American sectors), the expansion was related to the SED structure formation. The SED structure was registered from 15-17 UT on 17 March till 02 UT on 18 March. To highlight the SED structure impacts on positioning, we provide the snapshots of global maps of TEC, ROTI, and PPP errors with a mark of SED structure at 16:00-21:30 UT in Supplementary Material. It shows the SED development (as seen in TEC and ROTI) corresponded with the degradation of positioning. In contrast, in the Eastern Hemisphere (e.g., European and New Zealand sectors), it was due to auroral oval development. The structured ionospheric plasma inside the auroral oval developed during ~08-15 UT, causing intense irregularities. The PPP observations indicate that the development of those irregularities after ~12 UT significantly degraded the high-precision solutions.

Particularly, they caused ~12 hour outage of navigation solutions for numerous stations in the Southern hemisphere. The PPP outage is likely due to loss of signal lock to multiple scintillation satellite signals simultaneously, leading to less than 4 satellites available for positioning. Cherniak and Zakharenkova (2016) also noted serious degradation of GPS performance onboard Swarm satellites when they crossed the southern polar cap region. They found that at ~18 UT the tracked GPS satellite number suddenly decreased to less than 4. This effect was associated with SED/TOI structure occurrence in the SH, which was found to be stronger over the South America region than over North America for this particular storm. Prikryl et al. (2016) noted that the NH high-latitude scintillation during this storm was primarily enhanced in the cusp and SED regions, and in the auroral oval. The highest occurrence was collocated with strong ionospheric currents, particularly the poleward part of the westward electrojet or near the edge of the eastward electrojet regions.

Interhemispheric differences were found in terms of the impact of plasma irregularities on the PPP degradation, as can be concluded from Figures 5-7. This feature is related to the asymmetry in the dynamics of plasma irregularities between the two hemispheres. Cherniak and Zakharenkova (2016) attributed the asymmetry to changes in the IMF parameters. Using global multi-instrumental observations, Astafyeva et al. (2015) concluded that stronger effects of the ionospheric storm should occur in the SH, due to the presence of largely positive IMF By component. During the main phase of the storm, the IMF By became positive at 11 UT (see Figure 2a), and had positive values during 12-15 UT, as well as ~17-22:45 UT. When it was positive, there should be stronger upward field-aligned currents in the poleward region on the dusk side of the SH; the aurora should be brighter and more structured in the SH. In this case, more intense irregularities may occur with a strong density gradient that can cause severe scintillations of GPS signals. Our observation of the PPP degradation (see Figures 5-7) confirms the stronger effects in the SH.

## 3.3 Low-latitude disturbances and kinematic PPP error

At low latitudes, the storm-induced ionospheric plasma irregularities were not as significant as at high latitudes. Nevertheless, a considerable PPP degradation was observed on the storm day, over Asia-Australian (AA) and Central-South America (SA) regions. In this section, we investigate the storm-related ionospheric disturbance impacts on the kinematic PPP in details for these two sectors.

### 3.3.1 AA Sector

In the AA sector (30°S-30°N MLAT and 60°-160°E), we utilized observations from more than 200 GPS stations. Figure 8a and 8b illustrate ROTI distributions as functions of MLAT and UT and the PPP error distributions as a function of UT on 17-18 March 2015, respectively. On the storm recovery day, the ROTI was low and the position error was below 2 m. On the storm day during 07-12 UT (local daytime), while the ROTI enhancement was not apparent, the PPP error reached above 10 m. Figure 8b also included the TEC residuals (ΔTEC) during 07-12 UT to demonstrate the possible role of LSTIDs in the degradation of positioning over this sector. Figure 8c-8j presents the snapshots of ROTI and the PPP errors during 07:30-11:00 UT. The ROTI values are color-coded in the unit of TECU/min. PPP errors > 0.5 m at a station are represented as black circles and the circle size is proportional to the error magnitude. Significant PPP degradation during low ROTI values mainly occurred at ~30°N GLAT over the Chinese region, especially during 07:30-09:00 UT.

During the period of 07-12 UT, the AA sector was mainly on the dayside. The PPP degradation can be attributed to the EIA and other perturbations. Over this sector, the daytime EIA enhancement started after 06 UT as a consequence of eastward PEFs in response to southward turning of IMF Bz (Kuai et al., 2016, and their Figure 2). Subsequently, equatorward LSTIDs from the Southern to Northern Hemisphere were detected over the AA sector during 09-12 UT (Habarulema et al., 2018 and their Figure 3e). Several LSTIDs propagating from high to lower latitudes were observed around 09:40-11:20 UT in the East Asian sector (80°-140°E) (Liu et al., 2019), as also indicated by the variations of ΔTEC during 07-12 UT. The large PPP errors (>5 m) during 07-09 UT and 11-12 UT are associated with the TEC enhancement and LSTIDs, respectively.

The processes of EIA enhancement and LSTIDs during the storm are associated with rapid changes and sharp spatial gradients in TEC. Under those disturbed ionospheric conditions, the higher-order ionospheric effects become significant and cannot be not totally corrected by the ionospheric-free linear combination in our data processing, thus leading to the PPP degradation.

During the period of 14-18 UT (local night time), the most prominent enhancement in ROTI was observed at 5S°-25°N GLAT, which led to significant PPP errors (>5 m). The snapshots illustrated in Figure 8k-8r show that the PPP degradation was associated with the occurrence of EPIs over the Indian region, as evident in the increased ROTI intensity and the corresponding large PPP errors at 14:30-18:00 UT (local night) over the Indian sector, along the magnetic equator to middle latitudes.

At low latitudes, the post-sunset plasma irregularities (i.e., EPIs) were absent across most longitudes after SSC (see Movie S1). This observation agrees well with previous studies that reported suppressed EPIs during the March 2015 storm (e.g., Ramsingh et al., 2015; Carter et al., 2016; Zhou et al., 2016). It was suggested by those studies that the absence of post-sunset EPIs was due to the presence of disturbance dynamo electric fields (DDEFs) generated by the enhanced magnetic activity, as well as equatorward and westward directed winds. Those forces dominated for many hours in the post-sunset hours and suppressed the growth of R-T instability.

In contrast, the two cases of the severe post-sunset EPIs at the Australian and Indian sectors were associated with the storm-time PEFs that coincided with the local time of pre-reversal enhancement, which favors the growth of R-T instability that gives rise to EPIs (Ramsingh et al., 2015; Kil et al., 2016). Ramsingh et al. (2015) studied the ionospheric response over the Indian sector during the storm and reported a scintillation occurrence during 14-18 UT, extending from the equator to low latitude (~26.5°N). Ray et al. (2017) reported maximum position deviations of 5.2 m along the longitude direction during 15-16 UT on the storm day. These all support our extensive data analysis results that the post-sunset EPIs and associated scintillations caused salient degradation (even >10 m) in the high-precision GPS positioning over the Indian sector during 15-18 UT (Figure 8k-8r).

### 3.3.2 SA Sector

By exploiting observations from more than 100 GPS stations in the SA sector (30°S-30°N MLAT and 30°-90°W), Figures 9a and 9b illustrate the ROTI distribution dependence on MLAT and UT and the PPP error distributions as a function of UT on 17-18 March 2015, respectively. We note a typical occurrence of strong post-sunset EPIs over the region before the storm onset. After SSC, the ROTI values were quite low, but the position errors had a dramatic increase (even over 10 m) during 08-24 UT, particularly during the daytime period of 12-20 UT in this sector. The variations of ΔTEC during this period suggest the error increase was related to the development of LSTIDs . We note a strong suppression of post-sunset EPIs during a similar time (00-05 UT) for the next day in the recovery phase. However, after the storm, the ROTI variation revealed storm-induced plasma irregularities in the post-midnight/morning period of 08-12 UT. These irregularities caused up to a 10 m PPP error. A salient degradation was seen during the post-sunset period of 00-04 UT, but with low ROTI.

Figure 9c-9n shows snapshots of the ROTI variations and the PPP errors with a 30-min time resolution during the daytime period of 14:00-19:30 UT.  During this daytime period, the ROTI level was below 0.5 TECU/min. However, the position degradation occurred for the stations located at the magnetic equator, low, and beyond the EIA region. Specifically, at 14-15 UT, large position errors (>2 m) were registered near the equator and then at farther south low latitudes (Figure 9c-9e). The errors decreased at 15:30-16:00 UT (Figure 9f-9g), then increased again at 16:30-19:00 UT at low latitudes away from the equator (both north and south).

The development of notable PPP degradation (>5 m) before 20 UT (see Figures 9i-9n) is consistent with the EIA enhancement as reported by Venkatesh et al. (2017). The EIA anomaly was associated with PEFs at ~12 UT and a substorm onset at ~17:25 UT. Firstly, they associated PEFs effects to enhanced zonal electric fields during 12-14 UT and the F2 layer vertical expansion above the magnetic equator. According to Venkantesh et al. (2017, Figure 6), the EIA had a single-peak structure with enhanced TEC built-up, reaching its peak near the magnetic equator at ~16:30 UT. After 17:25 UT, a new enhancement of the zonal electric field led to a super fountain effect promoting the EIA trough (TEC depletion) which appeared above the magnetic equator and two crests over NA and SA. The EIA crest located at ~40°S in Brazil, which may be responsible for the notable position errors for the mid-latitude stations (e.g., 43.2°S) in SA, as shown in Figure 7i. The global maps of TEC and PPP errors in our supplementary material also indicate the possible role of the EIA enhancement in position degradation over this sector.

Apart from the storm-induced EIA intensification, multiple LSTIDs were registered in the daytime SA region (Zakharenkova et al., 2016). With an increase of auroral activity (AE exceeded 2000 nT) at 13-

14 UT, these LSTIDs were generated at auroral latitudes of both hemispheres during 14-16 UT. They propagated equatorward across the NA and SA sectors and merged near the magnetic equator, as indicated by the $\Delta\mathrm{TEC}$ variations in Figure 9. Some even propagated farther to the opposite hemisphere. We found a good agreement between LSTIDs fronts registered during 14-17 UT (Zakharenkova et al, 2016, Figure 5) and the location of the PPP degradation errors (Figures 9c-9j). It should be emphasized that the period of 14-16 UT corresponded to the local morning time when the EIA started to form with a single peak build-up, and it was also before the storm-induced intensification of the EIA with two distinct crest formations (after 17:25 UT). The large PPP degradation was observed at various locations within ±20° MLAT during that local morning time in the absence of ionospheric irregularities (ROTI, Figure 9) and in the absence of a developed two-crest EIA structure. This suggests that during 14-17 UT, multiple LSTIDs which propagated and merged near the magnetic equator during that particular time may also have contributed to the observed PPP degradation.

On the recovery day, post-midnight and morning (07-12 UT) EPIs were generated in the SA sector (see Figure 9b), which is consistent with that revealed by Zhou et al. (2016) and Carter et al. (2016). They suggested the formation of post-midnight EPIs was due to DDEFs effects and the storm-induced redistribution of plasma to higher altitudes, which created a steep plasma density gradient favoring the R-T instability. Our analysis reveals that occurrence of the post-midnight and morning EPIs also coincided with increased position errors over the region.

## 4. Summary and Conclusions

We present the first results of storm-induced ionospheric disturbance impacts on kinematic GPS PPP solutions during the geomagnetic storm of 17-18 March 2015 by analyzing an unprecedented number of ground-based GNSS stations (5500+) available worldwide. In this study, the ROTI metric was exploited as the representative indicator of the storm-induced plasma density irregularities. The results indicate that in addition to ionospheric irregularity impacts on the PPP degradation, other ionospheric disturbances may also contribute to the increased position errors or even position outage under storm conditions. The major findings from the global-scale analysis are summarized as follows:

(1) At high latitudes, the PPP solutions were degraded with intensified auroral activity during the two main phases of the storm, i.e., 7-12 UT and 14-23 UT. The most significant impacts were observed in the second main phase, during which southward turning of IMF Bz lasted for ~11 hours. At 16-18 UT, ~70% of high-latitude (50°-90°) GNSS stations were affected with a notable increase in their position error (>1 m).

(2) At high latitudes, the PPP degradation was associated with intense ionospheric plasma irregularities and SED/TOI structures. The degradation (>1 m) mostly happened where intense irregularities were observed, i.e., nightside equatorward edge and post-noon poleward side in the NH; late night and post-noon sides in the SH. The equatorward expansion of plasma irregularities led to the PPP degradation even at middle latitudes.

(3) Severe position errors (>10 m) were primarily seen around magnetic noon and midnight, which coincides well with expansion of the auroral oval of ionospheric irregularities and TOI structure occurrence from the dayside. The most notable impact is the PPP outage which occurred during the second main phase for high-latitude stations in the SH with a long-lasting outage period of ~ 12 hours. More severe impacts were seen in the SH, as compared with NH. The interhemispheric differences were probably related to the IMF orientation.

(4) At low latitudes, the PPP degradation is not only related to the dynamics of the post-sunset ionospheric plasma irregularities, but also the intensification of EIA and propagation of LSTIDs. The impact depended on longitudes or local time, and it was not as severe as at high latitudes.

(5) During 14-18 UT on the second main phase, the occurrence of PEF-induced post-sunset EPIs caused salient degradation (even >10 m) in the high-precision GPS positioning in the Indian sector. For the same period in the dayside American sector, the intensification of EIA and propagation of LSTID were most likely responsible for the PPP degradation.

Ionospheric disturbances during this severe storm are complex. Better indicators need to be developed to relate the ionospheric disturbances with the impact on navigation system performances. Further studies regarding the global impacts of other ionospheric disturbances, such as LSTID and SED/TOI should be carried out to attain a better understanding of the role that various ionospheric disturbances play in the degradation of GNSS applications when extreme space weather prevails.

## Acknowledgments

This work is supported by the Space Weather Technology, Research, and Education Center (SWx-TREC) at the University of Colorado Boulder and a grant (DI 9AC00009) provided by DARPA DSO Space Environment Exploitation (SEE) Program. The authors are grateful for the use of the raw GPS data provided by ARGN (ftp://ftp.ga.gov.au/geodesy-outgoing/gnss/data/daily/), RBMC (ftp://geoftp.ibge.gov.br/RBMC/), CACS (http:www.nrcan.gc.ca/home), CHAIN (ftp://chain.physics.unb.ca/gps/), International GNSS Monitoring & Assessment System (iGMAS) (http://www.igmas.org/) and CMONOC (http://www.neiscn.org/), CORS (ftp://geodesy.noaa.gov), EPN (ftp://olggps.oeaw.ac.at), IGN (ftp://rgpdata.ign.fr), IGS (ftp://cddis.gsfc. nasa.gov), RAMSAC CORS (www.igm.gov.ar/NuestrasActividades/Geodesia/Ramsac/), NOANET (www.gein.noa.gr), UNAVCO (ftp://data-out.unavco.org), and SOPAC (ftp://garner.ucsd.edu). All the derived GPS data for the present study can be accessed at the link http://doi.org/10.5281/zenodo.3733846. The authors thank the Space Weather Prediction Center of NOAA for the data of interplanetary parameters (ftp://sohoftp.nascom.nasa.gov/sdb/goes/ace/daily), and the World Data Center for Geomagnetism for the data of AE, SYM-H and the planetary index Kp (http://wdc.kugi.kyoto-u.ac.jp/index.html). Dr. Haitao Liu from Macau University of Science and Technology helped with processing TEC residuals. Dr. Shuli Song would like to thank National Key R&D Program of China (2016YFB0501503-3) and the key project of National Natural Science Fund (41730108). Dr. Zakharenkova was supported in part by RFBR grant 19-05-00570-A. The RTKLIB (version 2.4.2 p13) package can be accessed at this link http://www.rtklib.com/rtklib.htm.

## References

Abdu, M. (1997), Major phenomena of the equatorial ionosphere-thermosphere system under disturbed conditions, *Journal of Atmospheric and Solar-Terrestrial Physics*, 59(13), 1505-1519.

Abdu, M., E. Kherani, I. Batista, and J. Sobral (2009), Equatorial evening prereversal vertical drift and spread F suppression by disturbance penetration electric fields, *Geophysical Research Letters*, 36(19).

Afraimovich, E., E. Kosogorov, O. Lesyuta, and I. Ushakov (2001), Geomagnetic control of the spectrum of traveling ionospheric disturbances based on data from a global GPS network, *Radiophysics and quantum electronics*, 44(10), 763-773.

Astafyeva, E., I. Zakharenkova, and M. Förster (2015), Ionospheric response to the 2015 St. Patrick's Day storm: A global multi- instrumental overview, *Journal of Geophysical Research: Space Physics*, 120(10), 9023-9037.

Astafyeva, E., Y. Yasyukevich, A. Maksikov, and I. Zhivetiev (2014), Geomagnetic storms, super-storms, and their impacts on GPS-based navigation systems, *Space Weather*, 12(7), 508-525.

Basu, S., S. Basu, C. Valladares, H. C. Yeh, S. Y. Su, E. MacKenzie, P. Sultan, J. Aarons, F. Rich, and P. Doherty (2001), Ionospheric effects of major magnetic storms during the International Space Weather Period of September and October 1999: GPS observations, VHF/UHF scintillations, and in situ density structures at middle and equatorial latitudes, *Journal of Geophysical Research: Space Physics*, 106(A12), 30389-30413.

Basu, S., S. Basu, J. Makela, E. MacKenzie, P. Doherty, J. Wright, F. Rich, M. Keskinen, R. Sheehan, and A. Coster (2008), Large magnetic storm‐ induced nighttime ionospheric flows at midlatitudes and their impacts on GPS‐ based navigation systems, *Journal of Geophysical Research: Space Physics*, 113(A3).

Blewitt, G., C. Kreemer, W. C. Hammond, H. P. Plag, S. Stein, and E. Okal (2006), Rapid determination of earthquake magnitude using GPS for tsunami warning systems, *Geophysical Research Letters*, 33(11).

Buonsanto, M. J. (1999), Ionospheric storms—A review, *Space Science Reviews*, 88(3-4), 563-601.

Carter, B., E. Yizengaw, R. Pradipta, J. Retterer, K. Groves, C. Valladares, R. Caton, C. Bridgwood, R. Norman, and K. Zhang (2016), Global equatorial plasma bubble occurrence during the 2015 St. Patrick's Day storm, *Journal of Geophysical Research: Space Physics*, 121(1), 894-905.

Cherniak, I., and I. Zakharenkova (2016), High-latitude ionospheric irregularities: differences between ground- and space-based GPS measurements during the 2015 St. Patrick's Day storm, *Earth, Planets and Space*, 68(1), 136.

Cherniak, I., I. Zakharenkova, and R. J. Redmon (2015), Dynamics of the high-latitude ionospheric irregularities during the 17 March 2015St. Patrick's Day storm: Ground-based GPS measurements, *Space Weather*, 13(9), 585-597.

Cherniak, I., Krankowski, A., & Zakharenkova, I. (2014). Observation of the ionospheric irregularities over the Northern Hemisphere: Methodology and service. *Radio Science*, 49(8), 653–662. https://doi.org/10.1002/2014RS005433

Cherniak, I., Krankowski, A., & Zakharenkova, I. (2018). ROTI Maps: a new IGS ionospheric product characterizing the ionospheric irregularities occurrence. *GPS Solutions*, 22:69. https://doi.org/10.1007/s10291-018-0730-1

De Franceschi, G., L. Alfonsi, V. Romano, M. Aquino, A. Dodson, C. N. Mitchell, P. Spencer, and A. W. Wernik (2008), Dynamics of high-latitude patches and associated small-scale irregularities during the October and November 2003 storms, *Journal of Atmospheric and Solar-Terrestrial Physics*, 70(6), 879-888.

Ding, F., W. Wan, L. Liu, E. Afraimovich, S. Voeykov, and N. Perevalova (2008), A statistical study of large-scale traveling ionospheric disturbances observed by GPS TEC during major magnetic storms over the years 2003–2005, *Journal of Geophysical Research: Space Physics*, 113(A3).

Fejer, B. G., J. Jensen, T. Kikuchi, M. Abdu, and J. Chau (2007), Equatorial ionospheric electric fields during the November 2004 magnetic storm, *Journal of Geophysical Research: Space Physics*, 112(A10).

Figueiredo, C., C. Wrasse, H. Takahashi, Y. Otsuka, K. Shiokawa, and D. Barros (2017), Large‐ scale traveling ionospheric disturbances observed by GPS dTEC maps over North and South America on Saint Patrick's Day storm in 2015, *Journal of Geophysical Research: Space Physics*, 122(4), 4755-4763.

Gonzalez, W., J. A. Joselyn, Y. Kamide, H. W. Kroehl, G. Rostoker, B. Tsurutani, and V. Vasyliunas (1994), What is a geomagnetic storm?, *Journal of Geophysical Research: Space Physics*, 99(A4), 5771-5792.

Habarulema, J. B., E. Yizengaw, Z. T. Katamzi‐ Joseph, M. B. Moldwin, and S. Buchert (2018), Storm time global observations of large‐ scale TIDs from ground‐ based and in situ satellite measurements, *Journal of Geophysical Research: Space Physics*, 123(1), 711-724.

Heine, T. R., M. B. Moldwin, and S. Zou (2017), Small‐ scale structure of the midlatitude storm enhanced density plume during the 17 March 2015 St. Patrick's Day storm, *Journal of Geophysical Research: Space Physics*, 122(3), 3665-3677.

Heres, W., and N. A. Bonito (2007), An alternative method of computing altitude adjustment corrected geomagnetic coordinatesas applied to IGRF epoch 2005,Tech. Rep. AFRL-RV-HA-TR-2007-1190, Air Force Res. Lab., Space Vehicles Dir., Hanscom Air ForceBase, Mass. https://apps.dtic.mil/dtic/tr/fulltext/u2/a482074.pdf

Hocke, K., and K. Schlegel (1996), A review of atmospheric gravity waves and travelling ionospheric disturbances: 1982–1995, *Annales Geophysicae*, 14(9), 917-940.

Huang, C. S. (2018), Effects of Geomagnetic Storms on the Postsunset Vertical Plasma Drift in the Equatorial Ionosphere, *Journal of Geophysical Research: Space Physics*, 123(5), 4181-4191.

Jiao, Y., and Y. T. Morton (2015), Comparison of the effect of high-latitude and equatorial ionospheric scintillation on GPS signals during the maximum of solar cycle 24, *Radio Science*, 50(9), 886-903.

Jin, Y., J. I. Moen, and W. J. Miloch (2015), On the collocation of the cusp aurora and the GPS phase scintillation: A statistical study, *Journal of Geophysical Research: Space Physics*, 120(10), 9176-9191.

Kelley, M. C., J. J. Makela, O. de La Beaujardière, and J. Retterer (2011), Convective ionospheric storms: A review, *Reviews of Geophysics*, 49(2).

Kil, H., Lee, W. K., Paxton, L. J., Hairston, M. R., & Jee, G. (2016). Equatorial broad plasma depletions associated with the evening prereversal enhancement and plasma bubbles during the 17 March 2015 storm. *Journal of Geophysical Research: Space Physics*, 121, 5009–5021. https://doi.org/10.1002/2016JA023335

Kintner, P. M., B. M. Ledvina, and E. R. de Paula (2007), GPS and ionospheric scintillations, *Space Weather*, 5(9), doi: 10.1029/2006sw000260.

Kuai, J., L. Liu, J. Liu, S. Sripathi, B. Zhao, Y. Chen, H. Le, and L. Hu (2016), Effects of disturbed electric fields in the low- latitude and equatorial ionosphere during the 2015 St. Patrick's Day storm, *Journal of Geophysical Research: Space Physics*, 121(9), 9111-9126.

Li, G., B. Ning, Z. Ren, and L. Hu (2010a), Statistics of GPS ionospheric scintillation and irregularities over polar regions at solar minimum, *GPS Solutions*, 14(4), 331-341, doi: 10.1007/s10291-009-0156-x.

Li, G., B. Ning, L. Hu, L. Liu, X. Yue, W. Wan, B. Zhao, K. Igarashi, M. Kubota, and Y. Otsuka (2010b), Longitudinal development of low- latitude ionospheric irregularities during the geomagnetic storms of July 2004, *Journal of Geophysical Research: Space Physics*, 115(A4).

Li, J., G. Ma, T. Maruyama, and Z. Li (2012), Mid- latitude ionospheric irregularities persisting into late morning during the magnetic storm on 19 March 2001, *Journal of Geophysical Research: Space Physics*, 117(A8).

Liu, J., D.-H. Zhang, A. J. Coster, S.-R. Zhang, G.-Y. Ma, Y.-Q. Hao, and Z. Xiao (2019), A case study of the large-scale traveling ionospheric disturbances in the East Asian sector during the 2015 St. Patrick's Day geomagnetic storm, *Ann. Geophys. Discuss*., doi: https://doi.org/10.5194/angeo-2019-63, in review.

Liu, L., and W. Wan (2018), Chinese ionospheric investigations in 2016–2017, *Earth and Planetary Physics*, 2(2), 89-111.

Mannucci, A., B. Tsurutani, B. Iijima, A. Komjathy, A. Saito, W. Gonzalez, F. Guarnieri, J. Kozyra, and R. Skoug (2005), Dayside global ionospheric response to the major interplanetary events of October 29–30, 2003 "Halloween Storms", *Geophysical Research Letters*, 32(12).

Martinis, C., M. Mendillo, and J. Aarons (2005), Toward a synthesis of equatorial spread F onset and suppression during geomagnetic storms, *Journal of Geophysical Research: Space Physics*, 110(A7).

Mitchell, C. N., L. Alfonsi, G. De Franceschi, M. Lester, V. Romano, and A. Wernik (2005), GPS TEC and scintillation measurements from the polar ionosphere during the October 2003 storm, *Geophysical Research Letters*, 32(12).

Moen, J., K. Oksavik, L. Alfonsi, Y. Daabakk, V. Romano, and L. Spogli (2013), Space weather challenges of the polar cap ionosphere, *Journal of Space Weather and Space Climate*, 3, A02.

Morton, R. J. (2014), Investigation of the Impact of Solar Storms on the Global Positioning System Receivers at High Latitudes, paper presented at *Proceedings of the 2014 International Technical Meeting of The Institute of Navigation*, San Diego, California.

Nicolls, M. J., and M. C. Kelley (2005), Strong evidence for gravity wave seeding of an ionospheric plasma instability, *Geophysical research letters*, 32(5).

Ohta, Y., T. Kobayashi, H. Tsushima, S. Miura, R. Hino, T. Takasu, H. Fujimoto, T. Iinuma, K. Tachibana, and T. Demachi (2012), Quasi real- time fault model estimation for near- field tsunami forecasting based on RTK- GPS analysis: Application to the 2011 Tohoku- Oki earthquake (Mw 9.0), *Journal of Geophysical Research: Solid Earth*, 117(B2).

Pi, X., A. Mannucci, U. Lindqwister, and C. Ho (1997), Monitoring of global ionospheric irregularities using the worldwide GPS network, *Geophysical Research Letters*, 24(18), 2283-2286.

Prikryl, P., P. Jayachandran, S. Mushini, D. Pokhotelov, J. MacDougall, E. Donovan, E. Spanswick, and J.-P. St-Maurice (2010), GPS TEC, scintillation and cycle slips observed at high latitudes during solar minimum, *Annales Geophysicae* (09927689), 28(6).

Prikryl, P., R. Ghoddousi- Fard, J. Weygand, A. Viljanen, M. Connors, D. Danskin, P. Jayachandran, K. Jacobsen, Y. Andalsvik, and E. Thomas (2016), GPS phase scintillation at high latitudes during the geomagnetic storm of 17–18 March 2015, *Journal of Geophysical Research: Space Physics*, 121(10), 10,448-410,465.

Ramsingh, S. Sripathi, S. Sreekumar, S. Banola, K. Emperumal, P. Tiwari, and B. S. Kumar (2015), Low-latitude ionosphere response to super geomagnetic storm of 17/18 March 2015: Results from a chain of ground- based observations over Indian sector, *Journal of Geophysical Research: Space Physics*, 120(12), 10,864-810,882.

Ray, S., B. Roy, K. S. Paul, S. Goswami, C. Oikonomou, H. Haralambous, B. Chandel, and A. Paul (2017), Study of the effect of 17–18 March 2015 geomagnetic storm on the Indian longitudes using GPS and C/NOFS, *Journal of Geophysical Research: Space Physics*, 122(2), 2551-2563.

Richmond, A., and G. Lu (2000), Upper-atmospheric effects of magnetic storms: a brief tutorial, *Journal of Atmospheric and Solar-Terrestrial Physics*, 62(12), 1115-1127.

Tsugawa, T., A. Saito, and Y. Otsuka (2004), A statistical study of large- scale traveling ionospheric disturbances using the GPS network in Japan, *Journal of Geophysical Research: Space Physics*, 109(A6).

Tsunoda, R. T. (1988), High- latitude F region irregularities: A review and synthesis, *Reviews of Geophysics*, 26(4), 719-760.

Venkatesh, K., S. Tulasi Ram, P. Fagundes, G. K. Seemala, and I. Batista (2017), Electrodynamic disturbances in the Brazilian equatorial and low- latitude ionosphere on St. Patrick's day storm of 17 march 2015, *Journal of Geophysical Research: Space Physics*, 122(4), 4553-4570.

Wang, Y., Q. H. Zhang, P. Jayachandran, M. Lockwood, S. R. Zhang, J. Moen, Z. Y. Xing, Y. Z. Ma, and M. Lester (2016), A comparison between large- scale irregularities and scintillations in the polar ionosphere, *Geophysical Research Letters*, 43(10), 4790-4798.

Yang, Z., and Z. Liu (2018), Low- Latitude Ionospheric Density Irregularities and Associated Scintillations Investigated by Combining COSMIC RO and Ground- Based GPS Observations over a Solar Active Period, *Journal of Geophysical Research: Space Physics*, doi: 10.1029/2017JA024199.

Yao, Y., L. Liu, J. Kong, and C. Zhai (2016), Analysis of the global ionospheric disturbances of the March 2015 great storm, *Journal of Geophysical Research: Space Physics*, 121(12).

Zakharenkova, I., E. Astafyeva, and I. Cherniak (2016), GPS and GLONASS observations of large- scale traveling ionospheric disturbances during the 2015 St. Patrick's Day storm, *Journal of Geophysical Research: Space Physics*, 121(12).

Zhang, S. R., Y. Zhang, W. Wang, and O. P. Verkhoglyadova (2017), Geospace system responses to the St. Patrick's Day storms in 2013 and 2015, *Journal of Geophysical Research: Space Physics*, 122(6), 6901-6906.

Zhao, B., W. Wan, K. Tschu, K. Igarashi, T. Kikuchi, K. Nozaki, S. Watari, G. Li, L. Paxton, and L. Liu (2008), Ionosphere disturbances observed throughout Southeast Asia of the superstorm of 20–22 November 2003, *Journal of Geophysical Research: Space Physics*, 113(A3).

Zhou, Y. L., H. Lühr, C. Xiong, and R. F. Pfaff (2016), Ionospheric storm effects and equatorial plasma irregularities during the 17–18 March 2015 event, *Journal of Geophysical Research: Space Physics*, 121(9), 9146-9163.

Figure 1. Geographical distribution of GNSS stations. The black solid line indicates the magnetic equator.

Figure 2. Variations of (a) interplanetary and geomagnetic parameters (i.e., IMF By and Bz components, geomagnetic activity index Kp, SYM-H index, AE index); (b) horizontal errors and (c) vertical errors of kinematic PPP solutions on 17-18 March 2015. The shaded area and solid-color lines in (b) and (c) panels represent one-standard-error bands and mean of the solution errors, respectively. The dash line indicates the SSC at 4:45 UT.

Figure 3. Snapshots of a) global temporal-spatial variations of ROTI and b) kinematic 3-D PPP errors on 17-18 March 2015. The gray shading indicates nightside. The black solid line represents the magnetic equator.

Figure 4. (a) Corrected geomagnetic (CGM) latitude versus temporal distributions of a) ROTI, b) 3-D errors of kinematic PPP solutions, and c) percentage of GNSS stations with the 3-D position error exceeding 1 meter (red dot line for stations within geographic latitude 50°-90° while green solid line for remaining latitudes) and the AE index during 00-24 UT of 17-18 March 2015. The SSC time is represented by the black dash line. The separation between 17 and 18 March is indicated by the solid line.

Figure 5. Polar view maps of ROTI (a and d), 3-D PPP errors (b and e) and percentage of the 3-D error exceeding 1 meter (c and f) as well as the UT and MLT distributions of 3-D PPP errors (g and h) for the Northern Hemisphere on 17 March (a-c) and 18 March (d-f) 2015. Each polar view map covers 00-24 magnetic local time (MLT) and 40°-90°N CGM latitude. log (ocr) represents the logarithm of occurrence rates of the PPP errors in each bin (30 minutes) to the base 10.

Figure 6. Same as Figure 5, but for the Southern Hemisphere. Each polar view map covers 00-24 MLT and 40°-90°S CGM latitudes.

Figure 7. Time versus geographic latitude variations of ROTI along longitudes (c) 85°W in North America, (d) 10°E in Europe, (e) 65°W in South America and (f) 170°E in Australia during 00-24 UT of 17-18 March 2015. The variability of 3-D PPP errors for selected GPS stations (a and b) along each longitudinal sector is shown in the right panels (g, h, i and j, respectively). Labels on the right vertical axis of each panel indicate the CGM latitudes. The position results during the period of 12-24 UT for the selected stations in the SH (i and j) are highlighted with light blue color.

Figure 8. (a) CGM latitude versus UT distributions of ROTI and (b) distributions of 3-D PPP errors during 00-24 UT for 17-18 March 2015 and variations of ΔTEC within longitudes between 60°-160°E at 07-12 UT (dashed rectangle); (c-r) Snapshots of ROTI variations (colored squares) and 3-D PPP errors (>0.5m, black circles) during 07:30-11:00 and 14:30-18:00 UT on 17 March 2015 over Asian and Australian sector. The black solid line represents the magnetic equator.

Figure 9. (a) CGM latitude versus UT distributions of ROTI and (b) distributions of 3-D PPP errors during 00-24 UT for 17-18 March 2015 and ΔTEC variations within longitudes between 30°-90°W at 12-20 UT (dashed rectangle); (c-n) Snapshots of ROTI variations (colored squares) and 3-D PPP errors (>0.5m, black circles) during 14:00-19:30 UT on 17 March 2015 over Central and South American sector.

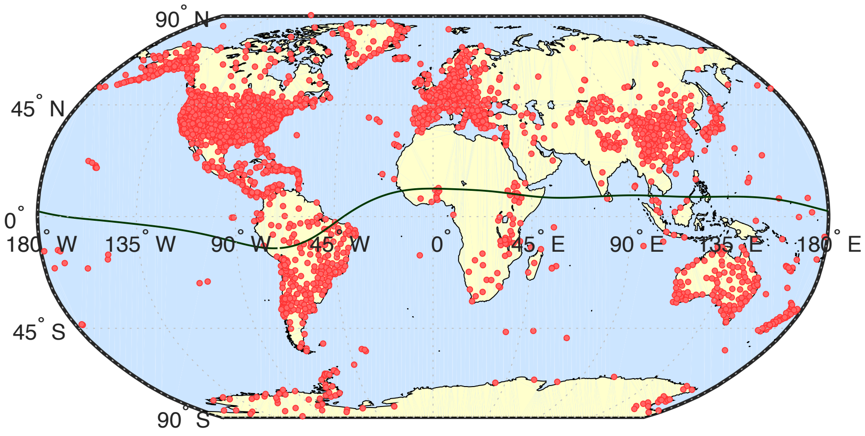
90° N
45° N
0°
45° S
90° S
180° W
135° W
90° W
45° W
0°
45° E
90° E
135° E
180° E

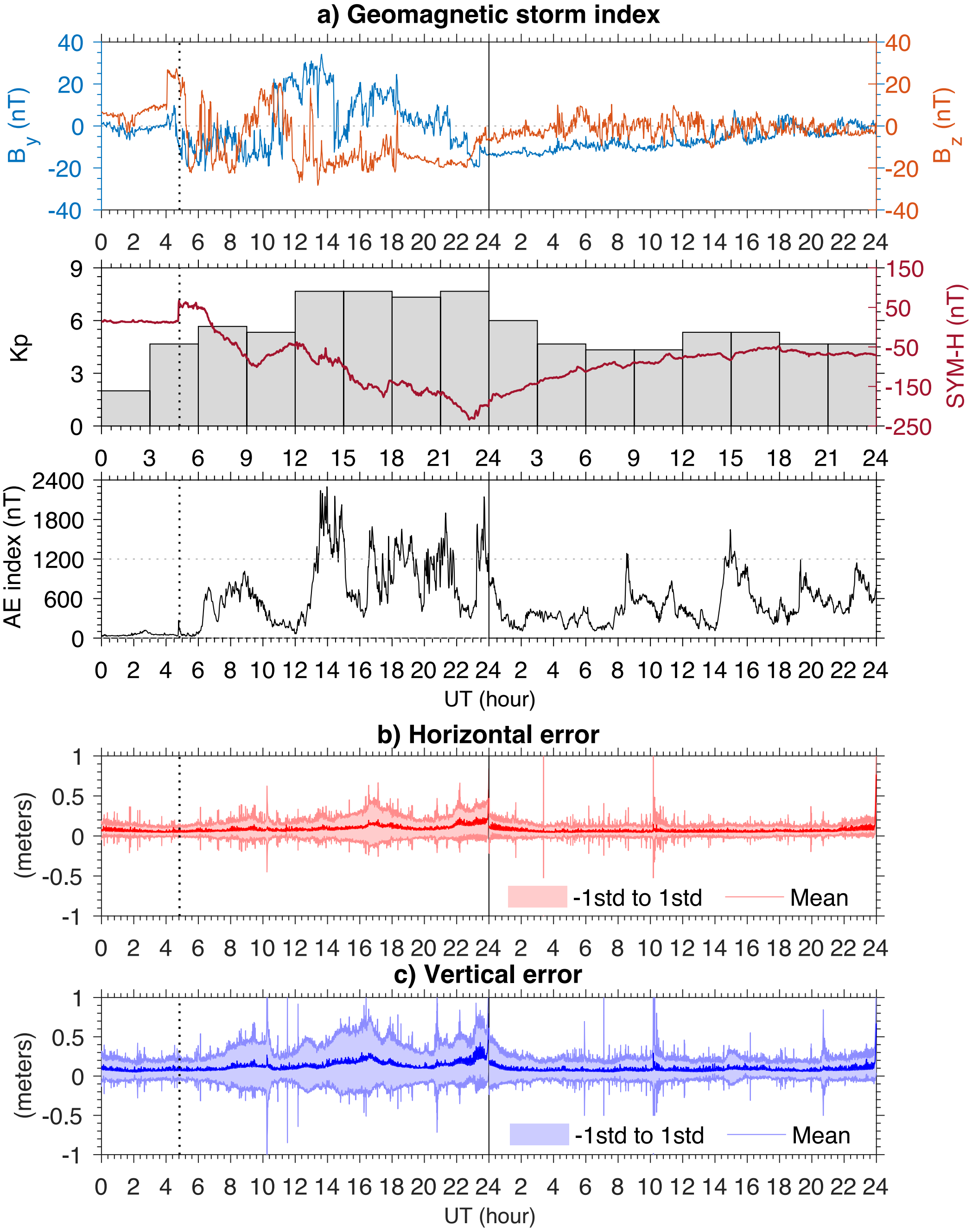
a) Geomagnetic storm index
B_y (nT)
B_z (nT)
40
20
0
-20
-40
0 2 4 6 8 10 12 14 16 18 20 22 24 2 4 6 8 10 12 14 16 18 20 22 24
Kp
SYM-H (nT)
9
6
3
0
150
50
-50
-150
-250
0 3 6 9 12 15 18 21 24 3 6 9 12 15 18 21 24
AE index (nT)
2400
1800
1200
600
0
0 2 4 6 8 10 12 14 16 18 20 22 24 2 4 6 8 10 12 14 16 18 20 22 24
UT (hour)
b) Horizontal error
(meters)
1
0.5
0
-0.5
-1
-1std to 1std
Mean
0 2 4 6 8 10 12 14 16 18 20 22 24 2 4 6 8 10 12 14 16 18 20 22 24
c) Vertical error
(meters)
1
0.5
0
-0.5
-1
-1std to 1std
Mean
0 2 4 6 8 10 12 14 16 18 20 22 24 2 4 6 8 10 12 14 16 18 20 22 24
UT (hour)

a) ROTI

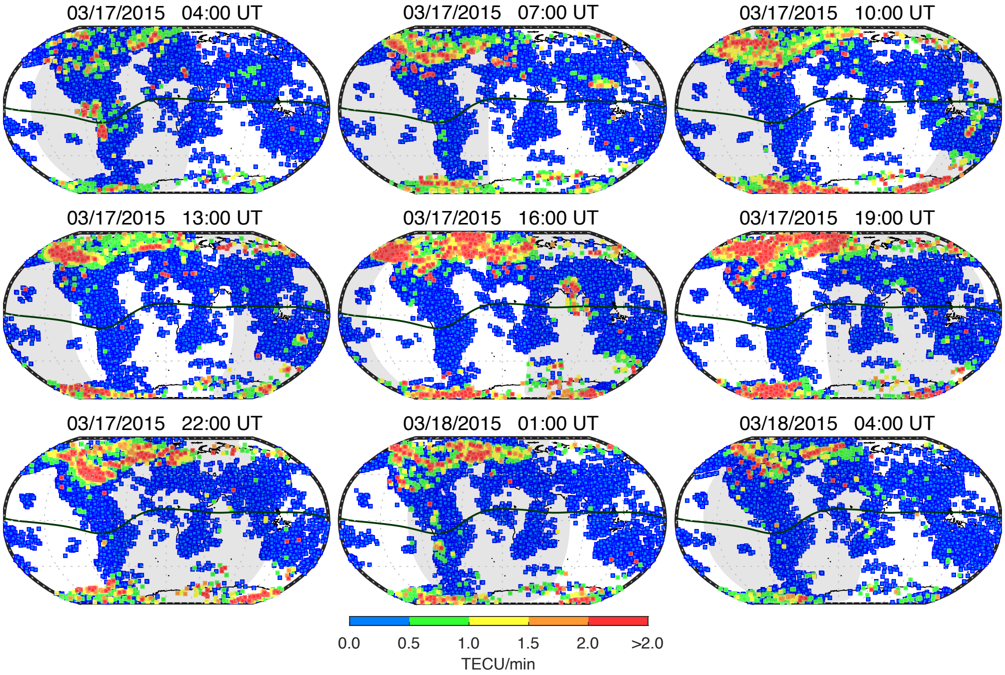

b) PPP error

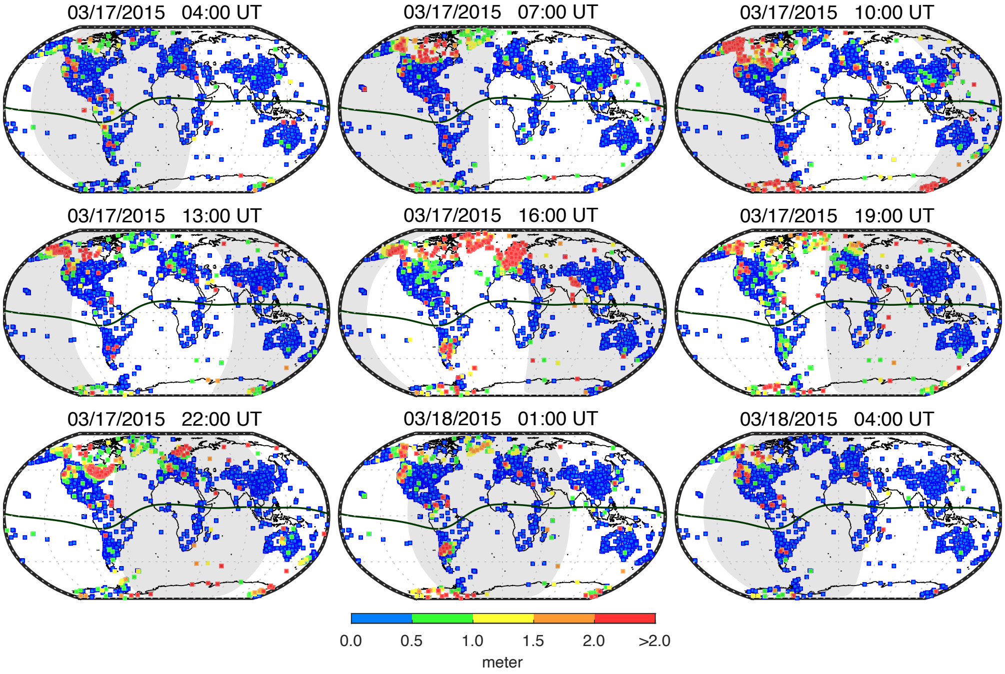

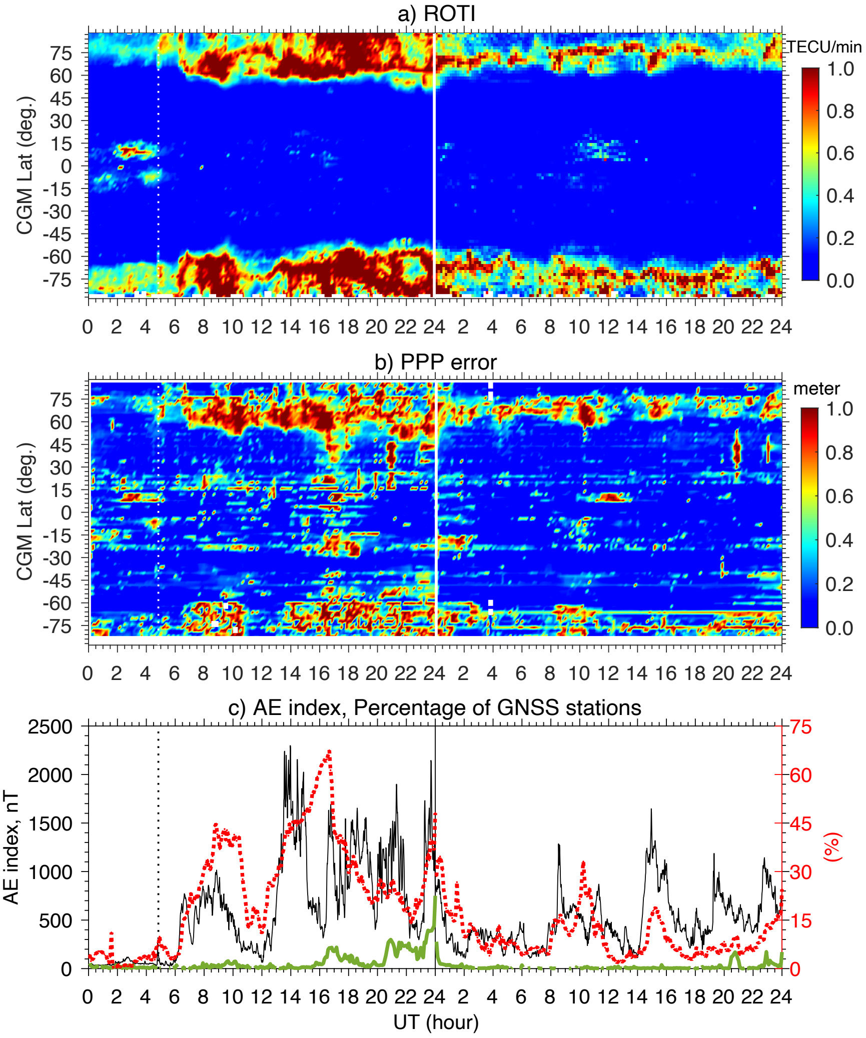
a) ROTI
CGM Lat (deg.)
75
60
45
30
15
0
-15
-30
-45
-60
-75
TECU/min
1.0
0.8
0.6
0.4
0.2
0.0
0 2 4 6 8 10 12 14 16 18 20 22 24 2 4 6 8 10 12 14 16 18 20 22 24
b) PPP error
CGM Lat (deg.)
meter
1.0
0.8
0.6
0.4
0.2
0.0
0 2 4 6 8 10 12 14 16 18 20 22 24 2 4 6 8 10 12 14 16 18 20 22 24
c) AE index, Percentage of GNSS stations
AE index, nT
2500
2000
1500
1000
500
0
(%)
75
60
45
30
15
0
0 2 4 6 8 10 12 14 16 18 20 22 24 2 4 6 8 10 12 14 16 18 20 22 24
UT (hour)

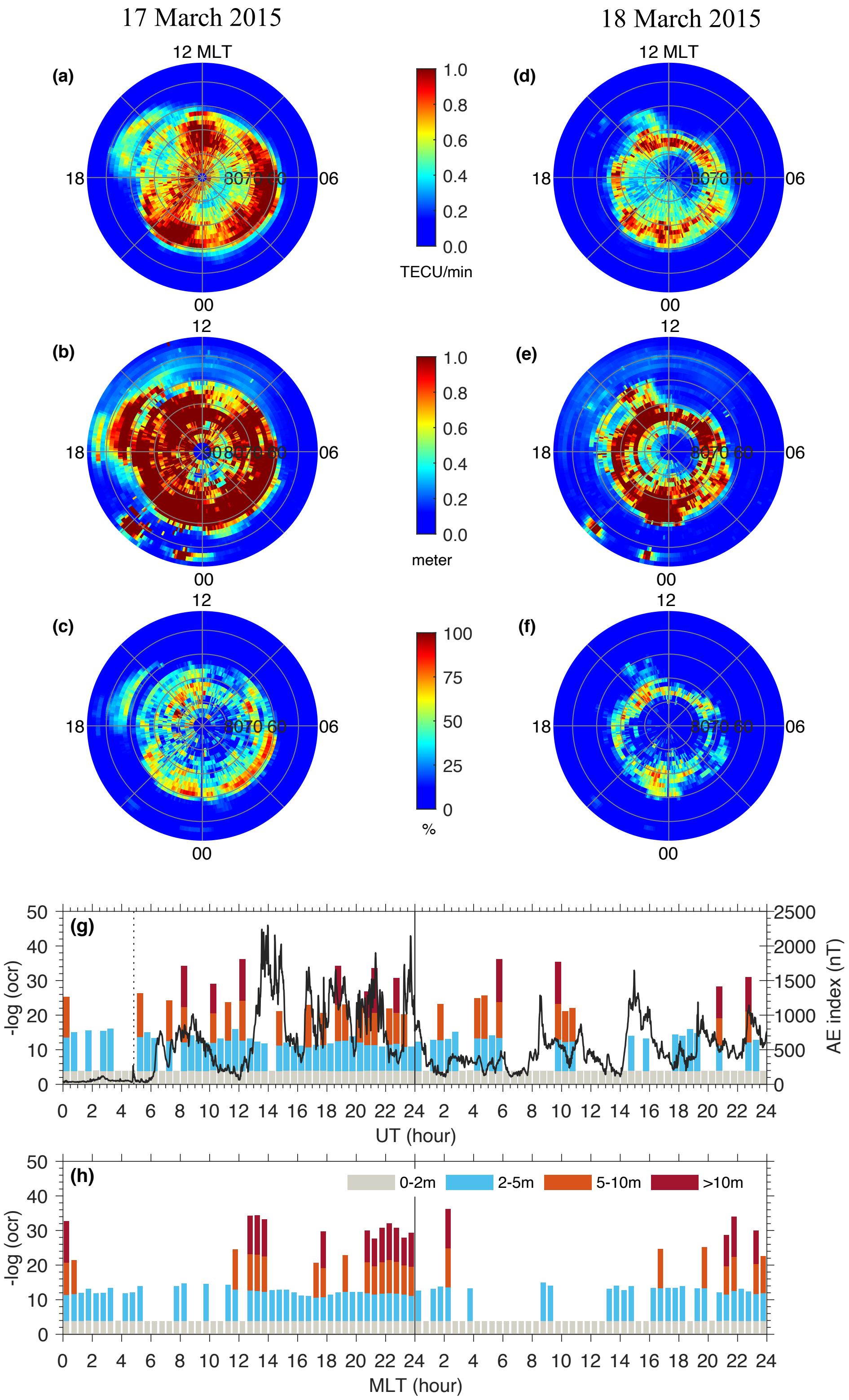
17 March 2015
18 March 2015
12 MLT
(a)
(d)
18
06
00
80 70 60
1.0
0.8
0.6
0.4
0.2
0.0
TECU/min
12
(b)
(e)
meter
(c)
(f)
100
75
50
25
0
%
(g)
-log (ocr)
AE index (nT)
2500
2000
1500
1000
500
UT (hour)
(h)
0-2m
2-5m
5-10m
>10m
MLT (hour)
50
40
30
20
10
0 2 4 6 8 10 12 14 16 18 20 22 24 2 4 6 8 10 12 14 16 18 20 22 24

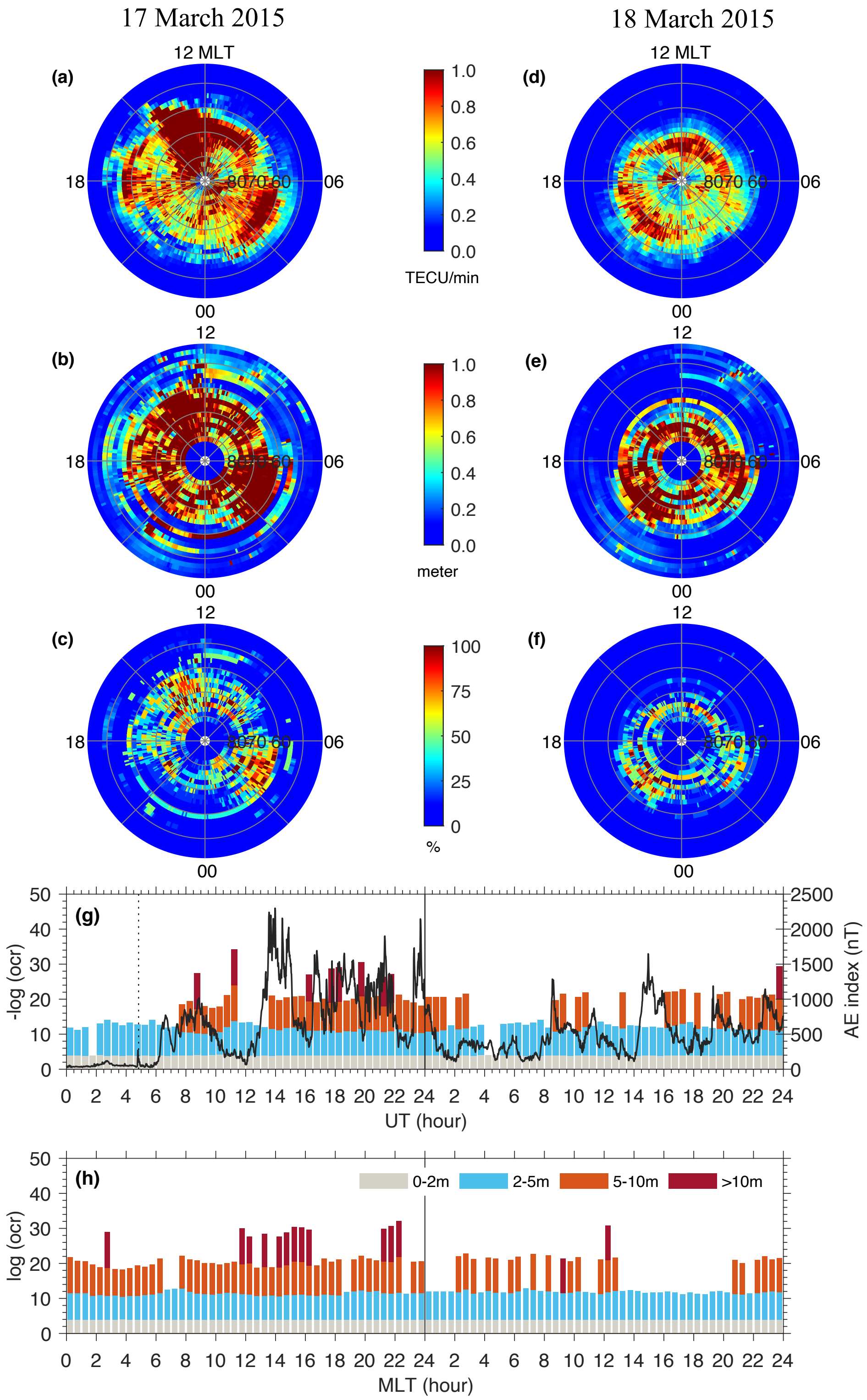
17 March 2015
18 March 2015
12 MLT
(a)
(d)
18
06
00
12
8070 60
1.0
0.8
0.6
0.4
0.2
0.0
TECU/min
(b)
(e)
meter
(c)
(f)
100
75
50
25
0
%
(g)
-log (ocr)
AE index (nT)
2500
2000
1500
1000
500
50
40
30
20
10
0
2 4 6 8 10 12 14 16 18 20 22 24
UT (hour)
(h)
0-2m
2-5m
5-10m
>10m
log (ocr)
MLT (hour)

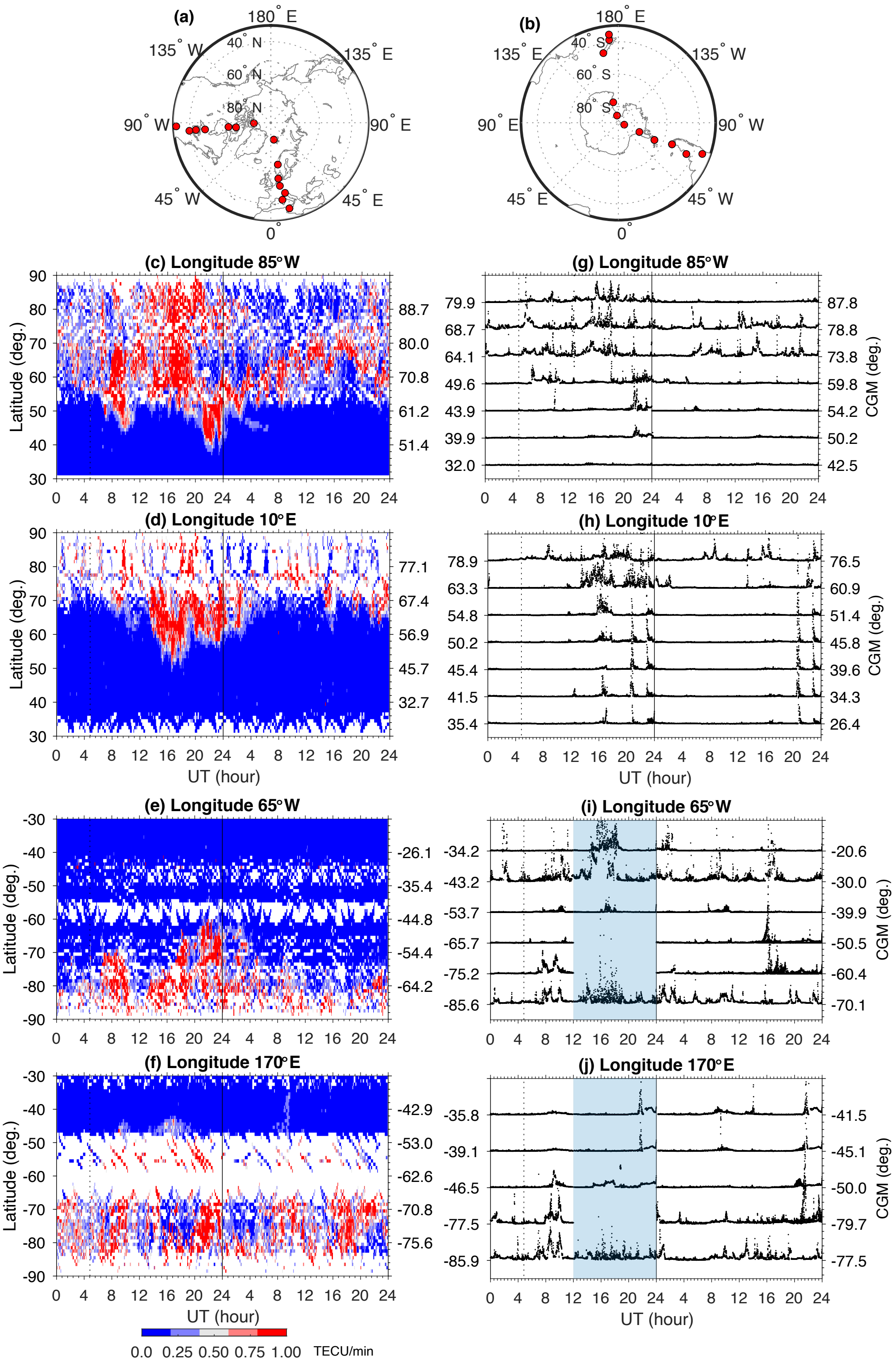
(a)
180° E
135° W
135° E
40° N
60° N
80° N
90° W
90° E
45° W
45° E
0°
(b)
180° E
135° E
135° W
40° S
60° S
80° S
90° E
90° W
45° E
45° W
0°
(c) Longitude 85°W
Latitude (deg.)
88.7
80.0
70.8
61.2
51.4
(d) Longitude 10°E
77.1
67.4
56.9
45.7
32.7
UT (hour)
(e) Longitude 65°W
-26.1
-35.4
-44.8
-54.4
-64.2
(f) Longitude 170°E
-42.9
-53.0
-62.6
-70.8
-75.6
0.0 0.25 0.50 0.75 1.00 TECU/min
(g) Longitude 85°W
79.9
68.7
64.1
49.6
43.9
39.9
32.0
87.8
78.8
73.8
59.8
54.2
50.2
42.5
CGM (deg.)
(h) Longitude 10°E
78.9
63.3
54.8
50.2
45.4
41.5
35.4
76.5
60.9
51.4
45.8
39.6
34.3
26.4
(i) Longitude 65°W
-34.2
-43.2
-53.7
-65.7
-75.2
-85.6
-20.6
-30.0
-39.9
-50.5
-60.4
-70.1
(j) Longitude 170°E
-35.8
-39.1
-46.5
-77.5
-85.9
-41.5
-45.1
-50.0
-79.7
-77.5
0 4 8 12 16 20 24 4 8 12 16 20 24

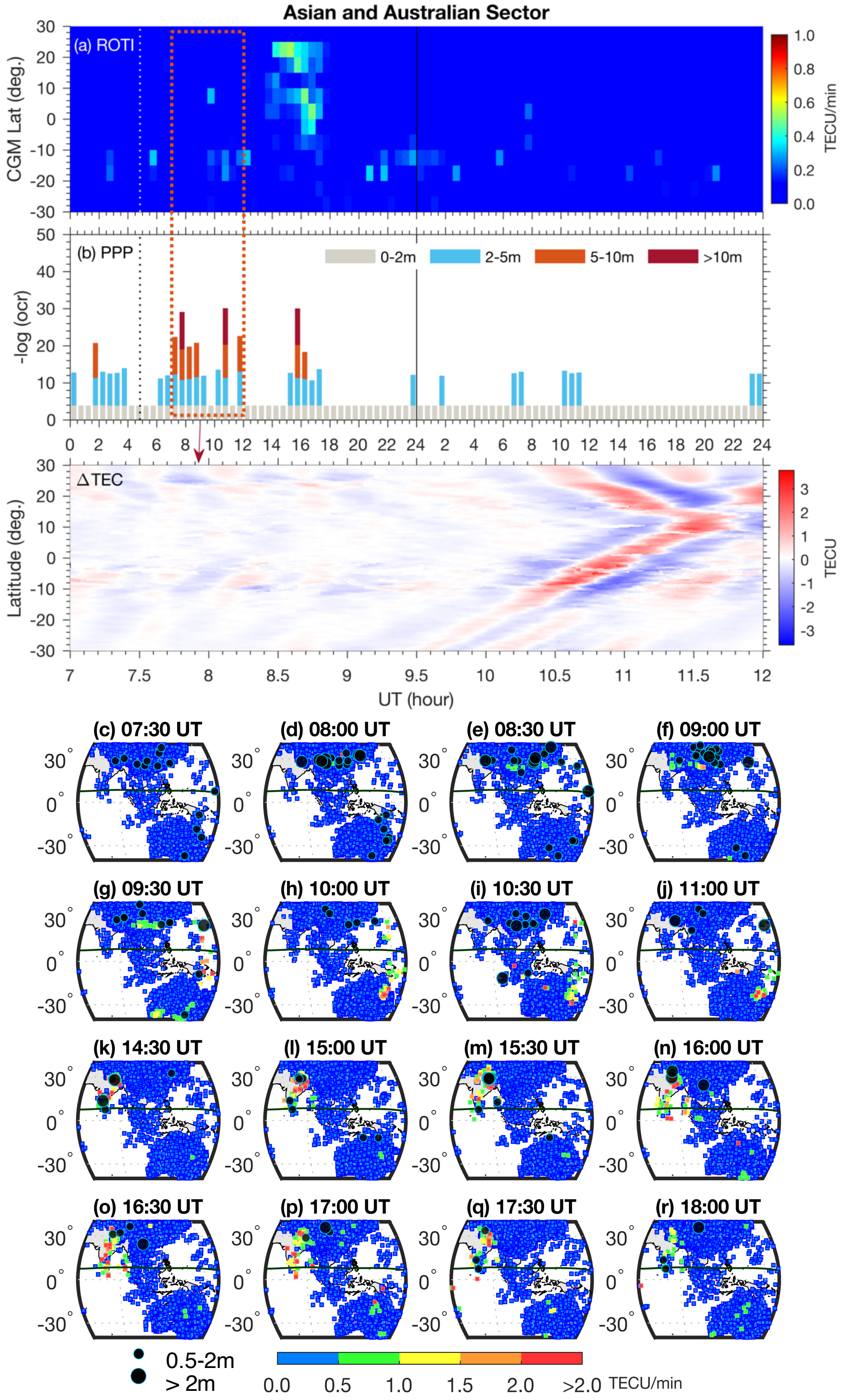
Asian and Australian Sector
(a) ROTI
CGM Lat (deg.)
30
20
10
0
-10
-20
-30
1.0
0.8
0.6
0.4
0.2
0.0
TECU/min
(b) PPP
-log (ocr)
50
40
30
20
10
0
0-2m
2-5m
5-10m
>10m
0 2 4 6 8 10 12 14 16 18 20 22 24 2 4 6 8 10 12 14 16 18 20 22 24
ΔTEC
Latitude (deg.)
3
2
1
0
-1
-2
-3
TECU
7 7.5 8 8.5 9 9.5 10 10.5 11 11.5 12
UT (hour)
(c) 07:30 UT
(d) 08:00 UT
(e) 08:30 UT
(f) 09:00 UT
(g) 09:30 UT
(h) 10:00 UT
(i) 10:30 UT
(j) 11:00 UT
(k) 14:30 UT
(l) 15:00 UT
(m) 15:30 UT
(n) 16:00 UT
(o) 16:30 UT
(p) 17:00 UT
(q) 17:30 UT
(r) 18:00 UT
30°
0°
-30°
0.5-2m
> 2m
0.0
0.5
1.0
1.5
2.0
>2.0
TECU/min

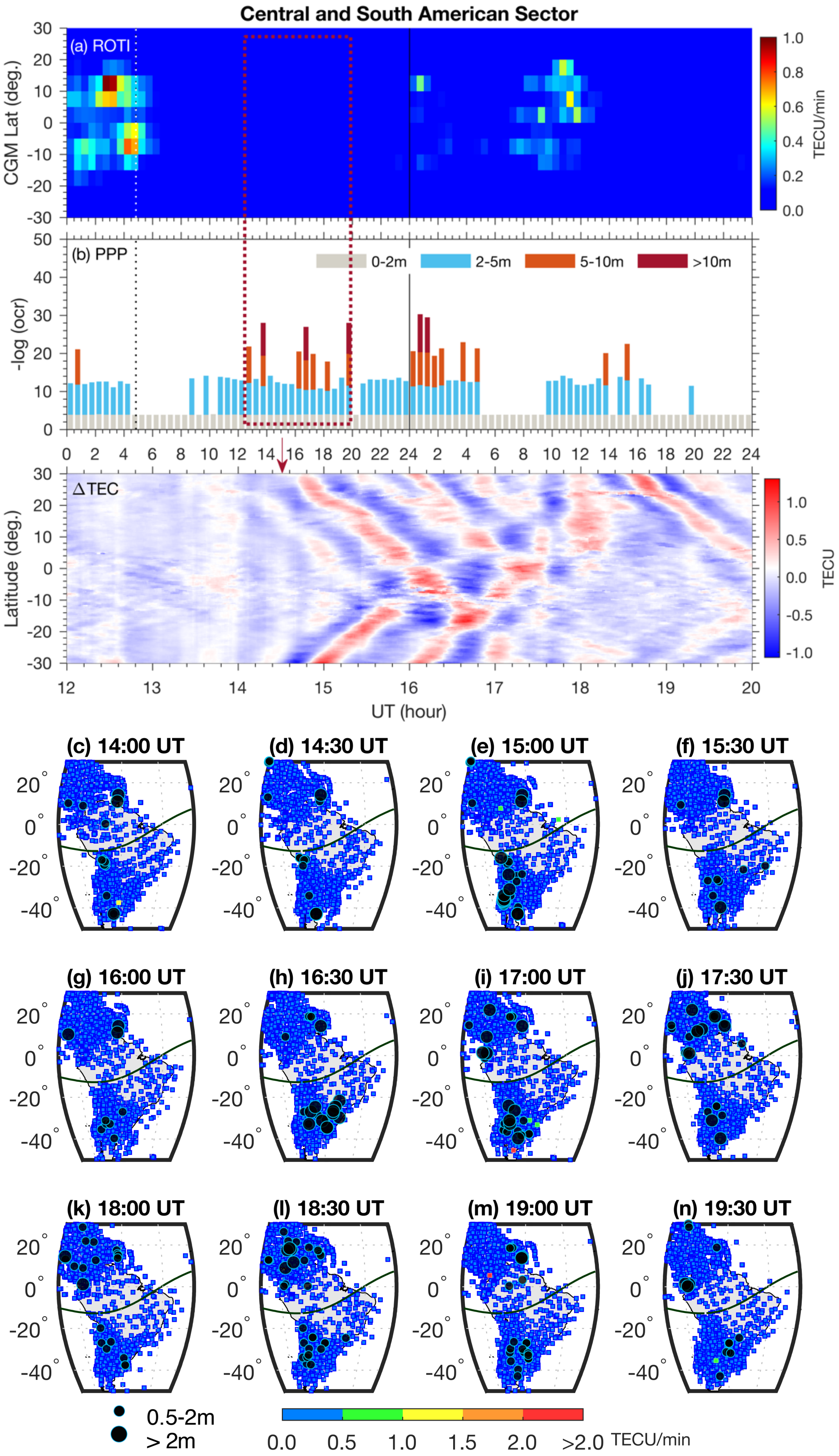
Central and South American Sector
(a) ROTI
CGM Lat (deg.)
TECU/min
(b) PPP
-log (ocr)
0-2m
2-5m
5-10m
>10m
0 2 4 6 8 10 12 14 16 18 20 22 24 2 4 6 8 10 12 14 16 18 20 22 24
ΔTEC
Latitude (deg.)
TECU
12 13 14 15 16 17 18 19 20
UT (hour)
(c) 14:00 UT
(d) 14:30 UT
(e) 15:00 UT
(f) 15:30 UT
(g) 16:00 UT
(h) 16:30 UT
(i) 17:00 UT
(j) 17:30 UT
(k) 18:00 UT
(l) 18:30 UT
(m) 19:00 UT
(n) 19:30 UT
0.5-2m
> 2m
0.0 0.5 1.0 1.5 2.0 >2.0 TECU/min